Okamoto *et al. Earth, Planets and Space (2018) 70:98*
https://doi.org/10.1186/s40623-018-0871-z

Earth, Planets and Space

EXPRESS LETTER

Open Access

Evaluation of accuracy of synthetic waveforms for subduction-zone earthquakes by using a land–ocean unified 3D structure model

Taro Okamoto[1*], Hiroshi Takenaka[2] and Takeshi Nakamura[3]

Abstract

Seismic wave propagation from shallow subduction-zone earthquakes can be strongly affected by 3D heterogeneous structures, such as oceanic water and sedimentary layers with irregular thicknesses. Synthetic waveforms must incorporate these effects so that they reproduce the characteristics of the observed waveforms properly. In this paper, we evaluate the accuracy of synthetic waveforms for small earthquakes in the source area of the 2011 Tohoku–Oki earthquake (M_{JMA} 9.0) at the Japan Trench. We compute the synthetic waveforms on the basis of a land–ocean unified 3D structure model using our heterogeneity, oceanic layer, and topography finite-difference method. In estimating the source parameters, we apply the first-motion augmented moment tensor (FAMT) method that we have recently proposed to minimize biases due to inappropriate source parameters. We find that, among several estimates, only the FAMT solutions are located very near the plate interface, which demonstrates the importance of using a 3D model for ensuring the self-consistency of the structure model, source position, and source mechanisms. Using several different filter passbands, we find that the full waveforms with periods longer than about 10 s can be reproduced well, while the degree of waveform fitting becomes worse for periods shorter than about 10 s. At periods around 4 s, the initial body waveforms can be modeled, but the later large-amplitude surface waves are difficult to reproduce correctly. The degree of waveform fitting depends on the source location, with better fittings for deep sources near land. We further examine the 3D sensitivity kernels: for the period of 12.8 s, the kernel shows a symmetric pattern with respect to the straight path between the source and the station, while for the period of 6.1 s, a curved pattern is obtained. Also, the range of the sensitive area becomes shallower for the latter case. Such a 3D spatial pattern cannot be predicted by 1D Earth models and indicates the strong effects of 3D heterogeneity on short-period ($\lesssim$ 10s) waveforms. Thus, it would be necessary to consider such 3D effects when improving the structure and source models.

Keywords: Japan Trench, Subduction-zone earthquake, Waveform inversion, GPU computing

Introduction

Seismic wave propagation from shallow subduction-zone earthquakes can be strongly affected by three-dimensionally heterogeneous structures, such as oceanic water and sedimentary layers with irregular thicknesses (e.g., Okamoto 2002; Nakamura et al. 2012, 2015). In waveform analyses of earthquake sources and structural heterogeneities, these effects due to three-dimensional (3D) heterogeneities must be properly incorporated in the synthetics, or otherwise the analyses could result in erroneous solutions (e.g., Okamoto and Takenaka 2009). Thus, we need to evaluate the accuracy of synthetic waveforms using a realistic 3D structure. Such studies require accurate source parameters and source locations. However, estimating these parameters for oceanic areas is often a challenge because of the presence of the above-mentioned 3D heterogeneities and the one-sided

*Correspondence: okamoto.t.ad@m.titech.ac.jp
[1] Department of Earth and Planetary Sciences, Tokyo Institute of Technology, 2-12-1 Ookayama, Meguro, Tokyo 152-8551, Japan
Full list of author information is available at the end of the article

distribution of seismic stations with respect to a trench (e.g., Okamoto 2002; Takemura et al. 2016). It is not satisfactory to address the problem by using only long-period waveforms, because surface waves are dominant in the long-period records, and therefore, the body waves, which provide information such as *P*-wave travel times to deal with the biases, become insignificant. To deal with this problem, we recently developed a method called first-motion augmented moment tensor (FAMT) analysis (Okamoto et al. 2017). FAMT analysis uses the initial part of the short-period waveforms in addition to the long-period full waveforms in order to augment the information based on the body wave first motions. The detailed source time function can also be inferred by using short-period waveforms (4–40 s).

In this paper, we investigate the accuracy of synthetic waveforms for small suboceanic earthquakes in the Japan Trench area, in connection with the 2011 Tohoku–Oki earthquake (M_{JMA} 9.0: Fig. 1a), as the effect of 3D heterogeneities on the waveforms would be different depending on the source location on the vast fault plane of the 2011 Tohoku–Oki earthquake.

Data

We selected two events whose hypocentral parameters determined by the Japan Meteorological Agency (JMA) are: 01/11/2003, 22:10:08.33 (JST), 37.7742°N, 143.2713°N, depth of 46 km, M_{JMA} 6.2 (M_{W}5.8), and 25/12/2007 23:04:32.85 (JST), 38.4833°E, 142.1537°N, depth of 40.29 km, M_{JMA} 5.6 (M_W6.1), respectively (Fig. 1a; the M_W values were taken from the Global Centroid Moment Tensor (GCMT) catalog). Both events had inter-plate thrust mechanisms and occurred in the source region of the 2011 Tohoku–Oki earthquake. The waveforms from the 01/11/2003 event (referred to as EV2003 hereafter) and the 25/12/2007 event (referred to as EV2007), respectively, represent examples of "basic" waveforms from shallow and deep parts of the fault responsible for the 2011 Tohoku–Oki earthquake. We also note that, with the exception of EV2003, inter-plate thrust earthquakes with magnitudes of about 6 or greater are sparse around the GCMT location, which represents the major source region of the 2011 Mw9.1 Tohoku–Oki earthquake (Fig. 1a). We used local full waveform data recorded at the K-NET, KiK-net, and F-net stations (Fig. 1a) operated by the National Research Institute for Earth Science and Disaster Resilience (NIED).

First-Motion Augmented Moment Tensor (FAMT) Analysis

In FAMT analysis, we combine a nonlinear waveform inversion method to estimate the moment tensor and the source time function of a point source

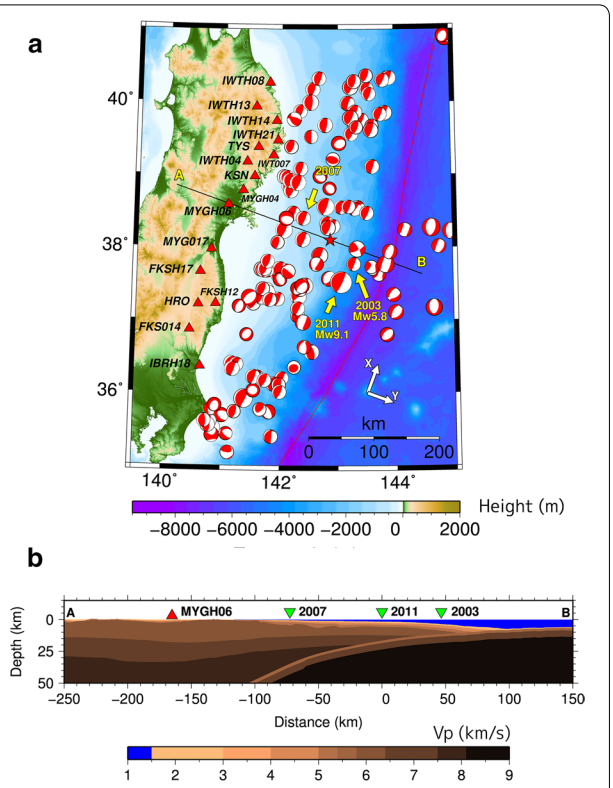

Fig. 1 **a** The study area: northeastern Japan and Japan Trench. The GCMT solutions in the oceanic area from 01/01/1996 to 30/09/2017 ($M_{\mathrm{W}} \geq 5.8$ and depth ≤ 50 km) are drawn. The GCMT solutions of the 01/11/2003 event (EV2003) and of the 25/12/2007 event (EV2007) are indicated by yellow arrows. The station locations are denoted by red triangles. The directions of the horizontal axes (*X* and *Y*) of the finite-difference grid are indicated by white arrows: the *X* axis is N20°E, and the *Y* axis is N110°E. **b** Example of a vertical cross section of the land–ocean unified 3D structure model: the cross section along the line *A–B* shown in **a** is displayed. Blue color denotes the ocean water layer. The epicenters of EV2003, EV2007, and the 2011 Tohoku–Oki earthquake (M_{JMA} 9.0) determined by JMA are projected (green triangles)

simultaneously with a space–time grid search method to infer the best point source position and origin time correction that minimize the squared residual:

$$F = \frac{1}{T}\sum_{i=1}^{N_W}\int_0^{T_i}\frac{[D_i(x_i,t)-S_i(x_i,t)]^2}{\left(\frac{1}{w_i}\sqrt{\frac{1}{T_i}\int_0^{T_i}[D_i(x_i,t)]^2\mathrm{d}t}\right)^2}\mathrm{d}t, \quad (1)$$

where $D_i(\boldsymbol{x}_i,t)$ and $S_i(\boldsymbol{x}_i,t)$ are the ith observed and synthetic waveforms, respectively, T_i is the length of the dataset, N_{W} is the number of waveforms, $T=\sum_{i=1}^{N_{\mathrm{W}}}T_i$, and w_i is weight on the ith datum (for details, see Okamoto et al. (2017) and its Additional file 1).

In the present analysis, as in Okamoto et al. (2017), passbands of 10–40 and 4–40 s are used for the

"long-period" and the "short-period" bandpass-filtered waveforms, respectively. The end time of the short-period waveforms is 10 s after onset of the P-wave, which is a sufficient duration to estimate the source time functions of the analyzed events. The weights (w_i in Eq. 1) are set to 3.0 for short-period waveforms and 1.0 for long-period waveforms. The space–time grid searches are performed on 3528 spatial grid points for EV2003 (21×21 in horizontal and 8 in vertical), and 7938 points for EV2007 (21×21 in horizontal and 18 in vertical), and on seven time points from -3 s to $+3$ s with an increment of 1 s for the origin time corrections. The spatial increments are 2.4 km in horizontal and 1.2 km in vertical, respectively, for both cases.

The synthetic waveforms, $S_i(\boldsymbol{x}_i, t)$ in Eq. (1), are composed of Green tensor generated with a triangular moment rate function with a width of 2 s. In order to incorporate the structural effects in the Green tensor, we use a land–ocean unified 3D structure model for the Japan Trench (Fig. 1b). This model was built from models of land–ocean topography (Kisimoto 2000), subsurface structures in the Japan Seismic Hazard Information Station V1 model (Fujiwara et al. 2009), the crust (Baba et al. 2006), the subducting Pacific plate (Baba et al. 2006), and the subducting Philippine Sea plate (Nakamura et al. 2010).

The Green tensor was computed using the same reciprocal method as in Okamoto et al. (2017), in which we applied our heterogeneity, oceanic layer, and topography (HOT)-FDM scheme (Nakamura et al. 2012) with the correct fluid–solid boundaries. The spatial grid interval and maximum frequency of the FDM simulations were 150 m and 0.611 Hz, respectively. The simulations were performed on the TSUBAME-2.5 and -3.0 supercomputers at the Tokyo Institute of Technology, Japan, using 150–640 graphic processing units (GPUs) as accelerators (Okamoto et al. 2010, 2013). For the details of the FDM parameters, see Additional file 1: Table S1.

Results of FAMT Analysis

We find that the best origin time correction to the JMA origin times is 0 s for both events (Additional file 1: Fig. S1). The inferred FAMT parameters are listed in Table S2 and S3 in Additional file 1. For both EV2003 and EV2007, the distributions of the residuals (F in Eq. 1) display well-defined spatial minimums (Fig. 2a, b). In the case of EV2003, the reddish area with small residuals is confined to layer 2 of the oceanic crust, and in the case of EV2007, the upper limit of the reddish area is nearly along the inclined plate interface: these features show the sensitivity of the waveforms to the source positions in the 3D model. In both cases, the FAMT locations are almost at the plate interface of the 3D model and are thus consistent with the inter-plate mechanisms of these events. Figure 2c, d compares various estimated source depths: the GCMT and the JMA-CMT are based on waveforms with periods of 40 s or longer, and the F-net MT is based on waveforms with periods of 20 s or longer. Along with these routinely determined solutions are plotted the positions of LPMT (long-period MT) that denote the best locations of the point moment tensor sources determined in this study by using the same procedure as in the FAMT analysis but with only the long-period (10–40 s) data. The estimates based on the long-period waveforms tend to be deeper than the plate interface (except the JMA-CMT of EV2003). It is unlikely that these differences in the estimated depths are the result of the source finiteness, as the fault planes are considered to be located along the plate interface. Thus, we consider that these differences are caused by the differences between the assumed structures of the respective analyses and by the degraded resolution of the long-period (long-wavelength) signals. The FAMT solutions demonstrate the importance of the 3D structure for ensuring the "self-consistency" of the structure model, source locations, and source mechanisms. The horizontal scatter of the source locations is within a few kilometers for EV2003 and within 20 km for EV2007 (Additional file 1: Fig. S2).

Figure 3 compares the observed velocity waveforms with the synthetics determined in the FAMT analyses. The synthetic waveforms fit the observed waveforms generally well in both cases. The simple short-period waveforms (the initial *P*-waves) of EV2003 are well reproduced with an approximately triangular source time function. On the other hand, a somewhat complex source time function is estimated for EV2007 on the basis of the multiple (split) peaks in the observed short-period waveforms.

We compare the observed waveforms with the synthetics computed using the 3D model and a flat-layered (1D) structure model for a period band of 10–40 s in Fig. 3c, d. The 1D synthetics were computed using the 1D structure model listed in Table 3 of Wu et al. (2008) and the discrete wavenumber method program (Takeo 1985) with the FAMT parameters. The 1D model was constructed for the analysis of the 1978 and 2005 Miyagi–Oki earthquakes that occurred near the coast; thus, the fit of the 1D synthetics to the observations is better for EV2007 (Fig. 3d) than for EV2003 (Fig. 3c). The land-based 1D structure model is not appropriate for EV2003, which occurred far off the coast; this can be seen from the large misfit of the 1D synthetic surface wave packets to the observations. Even for EV2007, the major phases (surface waves) show phase shifts and amplitude mismatches relative to the observations, even in the applied long-period band (10–40 s).

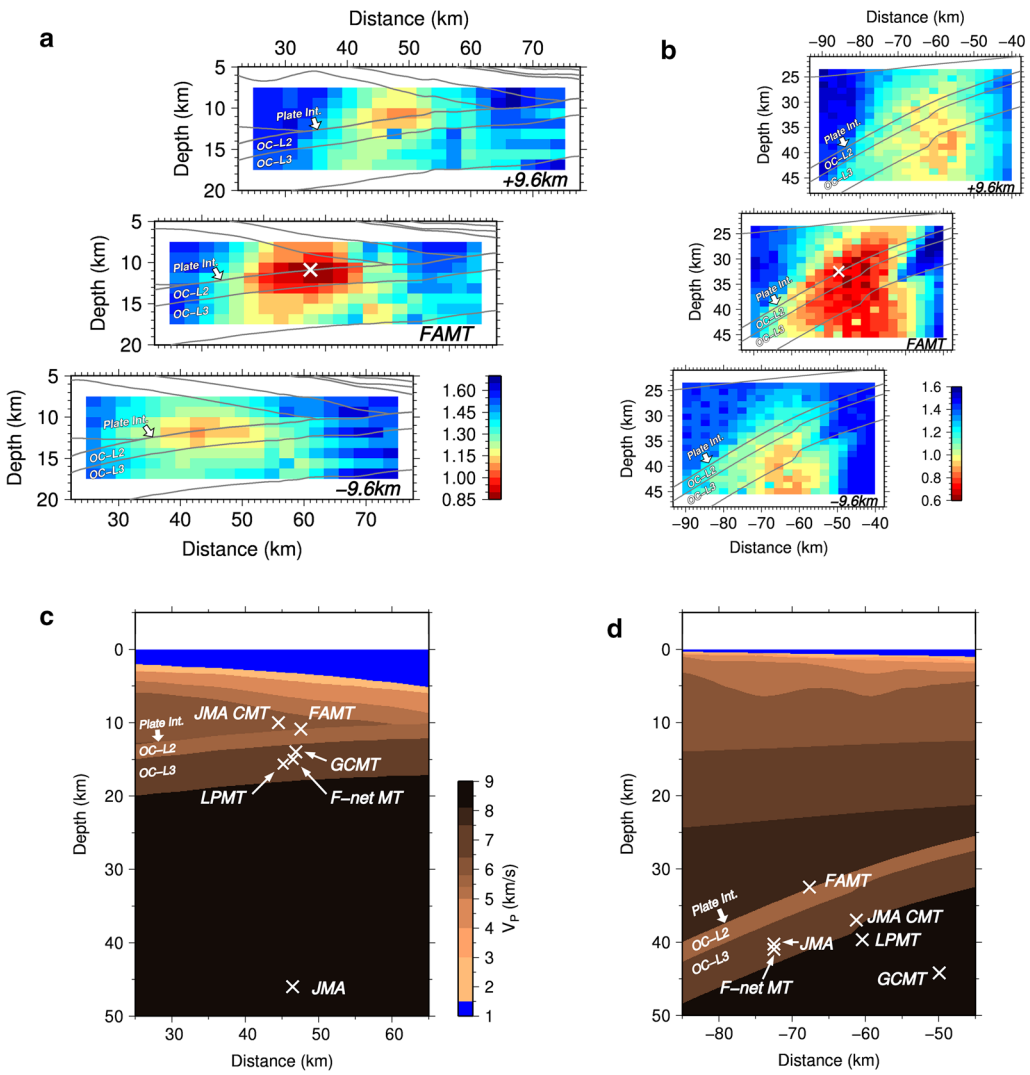

Fig. 2 **a** Vertical cross sections of the spatial distribution of the residual (Eq. 1) for EV2003 obtained by the spatial grid search performed with the best (0 s) origin time correction. The cross section through the best (FAMT) source position (middle), the cross section shifted from the middle one in the positive *X* direction by 9.6 km (top), and the cross section shifted from the middle one in the negative *X* direction by 9.6 km (bottom) are shown. Red corresponds to the small (good) residuals, and the best point is indicated by the white cross on the middle figure. Gray curves denote the interfaces of the 3D structure model. The plate interface (Plate Int.), layer 2 (OC-L2), and layer 3 (OC-L3) of the oceanic crust are indicated. **b** Same as **a** but for EV2007. **c** Various results of source position estimations for EV2003. The JMA hypocenter (JMA) and the positions of the F-net MT (best depth of a point moment tensor), the GCMT and the JMA-CMT (best locations of the centroids), and the FAMT (this study) are projected on the best cross section displayed in **a**. The "LPMT" (long-period MT) determined in this study is also projected (see text). **d** Same as **c** but for EV2007

(See figure on next page.)

Fig. 3 **a** Observed and synthetic waveforms for EV2003. The top trace in each pair, denoted DATA, is the observed ground velocity waveform; the bottom trace, denoted as SYN, is the corresponding synthetic computed for the FAMT parameters. The horizontal components with respect to the FDM grid are used in the FAMT analysis so that the last characters *X* and *Y* in the component name denote the directions of the horizontal ground motions (Fig. 1a). The character U denotes upward ground motion. The first two columns from TYS-X to HRO-U display the short-period waveforms with a passband of 4–40 s; the remaining columns display the long-period waveforms with a passband of 10–40 s. The numbers next to each pair denote the maximum amplitude (10^{-3} cm/s) of the observed waveform. The estimated moment magnitude and the normalized residual (*F* in Eq. 1) are shown at the top. The obtained source time function (STF) and the moment tensor are also plotted in the bottom-right corner. **b** Same as **a** but for EV2007. **c** Detailed comparisons of the observed velocity waveforms (DATA: red) and the synthetic waveforms computed using 3D (blue) and a flat-layered structure model (1D: gray) at station TYS and HRO. **d** Same as **c** but for EV2007

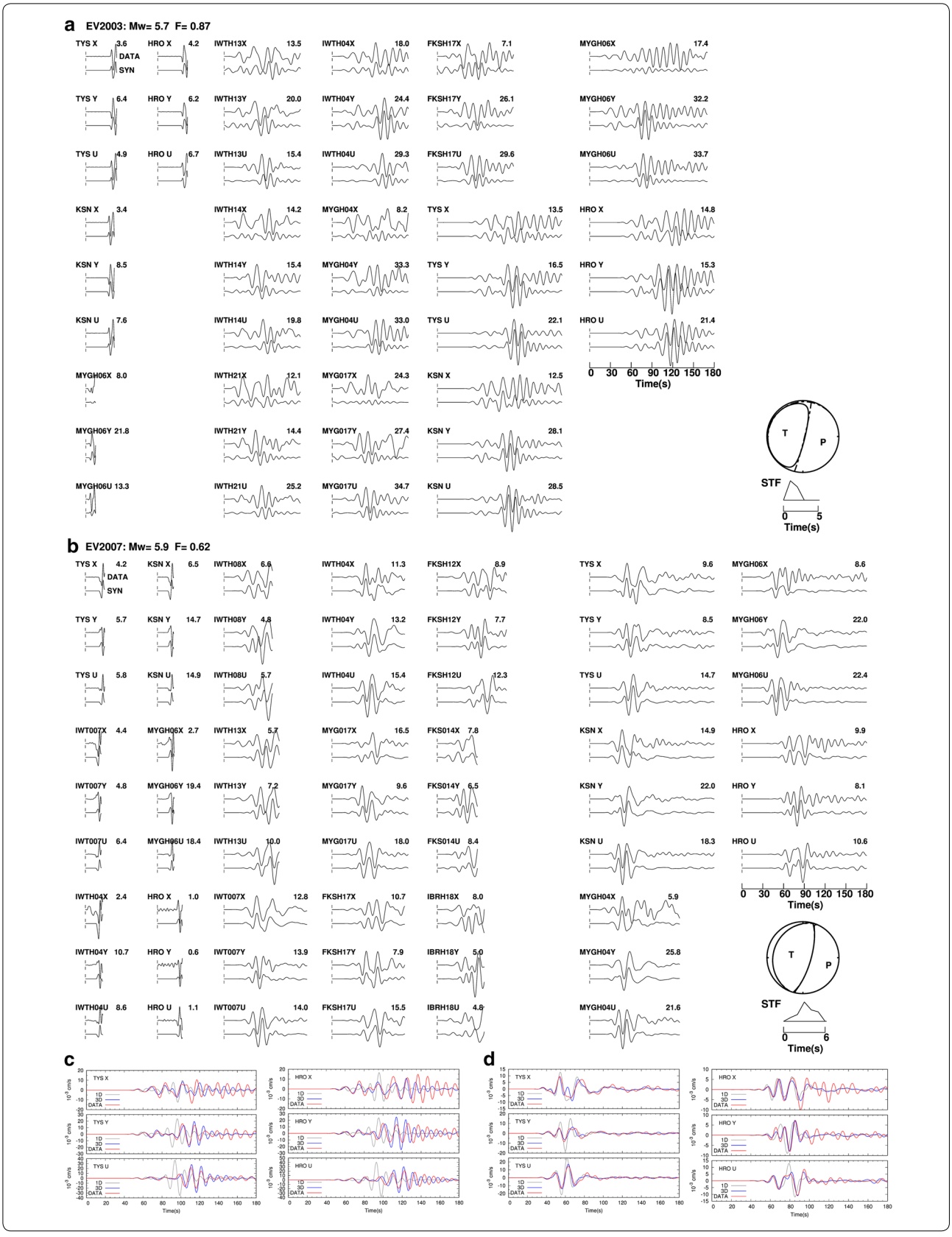
a
EV2003: Mw= 5.7 F= 0.87
TYS X 3.6
HRO X 4.2
DATA
SYN
IWTH13X 13.5
IWTH04X 18.0
FKSH17X 7.1
MYGH06X 17.4
TYS Y 6.4
HRO Y 6.2
IWTH13Y 20.0
IWTH04Y 24.4
FKSH17Y 26.1
MYGH06Y 32.2
TYS U 4.9
HRO U 6.7
IWTH13U 15.4
IWTH04U 29.3
FKSH17U 29.6
MYGH06U 33.7
KSN X 3.4
IWTH14X 14.2
MYGH04X 8.2
TYS X 13.5
HRO X 14.8
KSN Y 8.5
IWTH14Y 15.4
MYGH04Y 33.3
TYS Y 16.5
HRO Y 15.3
KSN U 7.6
IWTH14U 19.8
MYGH04U 33.0
TYS U 22.1
HRO U 21.4
MYGH06X 8.0
IWTH21X 12.1
MYG017X 24.3
KSN X 12.5
MYGH06Y 21.8
IWTH21Y 14.4
MYG017Y 27.4
KSN Y 28.1
MYGH06U 13.3
IWTH21U 25.2
MYG017U 34.7
KSN U 28.5
0 30 60 90 120 150 180
Time(s)
T
P
STF
0 5
Time(s)
b
EV2007: Mw= 5.9 F= 0.62
TYS X 4.2
KSN X 6.5
IWTH08X 6.6
IWTH04X 11.3
FKSH12X 8.9
TYS X 9.6
MYGH06X 8.6
DATA
SYN
TYS Y 5.7
KSN Y 14.7
IWTH08Y 4.8
IWTH04Y 13.2
FKSH12Y 7.7
TYS Y 8.5
MYGH06Y 22.0
TYS U 5.8
KSN U 14.9
IWTH08U 5.7
IWTH04U 15.4
FKSH12U 12.3
TYS U 14.7
MYGH06U 22.4
IWT007X 4.4
MYGH06X 2.7
IWTH13X 5.7
MYG017X 16.5
FKS014X 7.8
KSN X 14.9
HRO X 9.9
IWT007Y 4.8
MYGH06Y 19.4
IWTH13Y 7.2
MYG017Y 9.6
FKS014Y 6.5
KSN Y 22.0
HRO Y 8.1
IWT007U 6.4
MYGH06U 18.4
IWTH13U 10.0
MYG017U 18.0
FKS014U 8.4
KSN U 18.3
HRO U 10.6
IWTH04X 2.4
HRO X 1.0
IWT007X 12.8
FKSH17X 10.7
IBRH18X 8.0
MYGH04X 5.9
IWTH04Y 10.7
HRO Y 0.6
IWT007Y 13.9
FKSH17Y 7.9
IBRH18Y 5.0
MYGH04Y 25.8
IWTH04U 8.6
HRO U 1.1
IWT007U 14.0
FKSH17U 15.5
IBRH18U 4.8
MYGH04U 21.6
0 30 60 90 120 150 180
Time(s)
T
P
STF
0 6
Time(s)
c
TYS X
HRO X
TYS Y
HRO Y
TYS U
HRO U
1D
3D
DATA
Time(s)
d
TYS X
HRO X
TYS Y
HRO Y
TYS U
HRO U
1D
3D
DATA
Time(s)

Waveform fitting

To evaluate the degree of waveform fitting, we compare the observed and synthetic waveforms with several passbands. Figure 4a, b plots waveforms from two selected stations (TYS and HRO; all the waveforms are plotted in Additional file 1: Figs. S3 and S4). In these analyses, the FAMT parameters are used to generate synthetic waveforms; in so doing, the biases due to inappropriate source mechanisms and locations are minimized. For the shortest passband (2–4 s), the observed waveforms show prolonged ground motions in some components (e.g., HRO in Fig. 4b and MYGH06 in Additional file 1: Fig. S3a), but the corresponding synthetics do not reproduce such characteristics. For the passbands of 4–7 and 7–10 s, which are included in the passband of the "short-period" waveforms in the FAMT analysis, the later large-amplitude surface waves are not well reproduced by the synthetics, while the body waveforms of the initial *P*-waves are reproduced (Fig. 3). The observed waveforms with periods of around 10 s or longer, especially the major part of the surface wave packets, are generally well reproduced, as shown in the fourth pairs of Fig. 4a, b.

Figure 4c, d plots the normalized residuals (F in Eq. 1) computed using the full waveforms of the 33 components in the case of EV2003 and the full waveforms of the 42 components in the case of EV2007, respectively. Here, we set all the weights to 1.0 in order that a residual value of 1.0 is assigned to a synthetic trace with "null" (zero) amplitude: that is, a residual larger than 1 (depicted with green lines in Fig. 4c, d) indicates a synthetic worse than the "null trace." For both events, the residuals for passbands shorter than 10 s are larger than 1, while those for passbands longer than 10 s are smaller than 1: these values indicate that the synthetics with periods shorter than 10 s do not fit the corresponding observations, as described above. The residual of the 4–40 s passband also exceeds 1 for EV2003, while it is (slightly) smaller than 1 for EV2007, which shows that the synthetics with the 4–40 s passband fit the observations to some extent for the latter event. This fit can be visually verified in Fig. 4b (bottom pairs of traces) and in Additional file 1: Fig. S4e. We consider that this difference between EV2003 and EV2007 is due to the different source locations: the EV2007 event occurred close to land at a relatively deep plate interface, where the effect of heterogeneous shallow structures would be weaker than in the case of EV2003, which occurred far off the coast at a shallow plate interface.

We note that the normalized residual depends on the selected time window. Limiting the time window to the body wave part dramatically reduces the residuals (Additional file 1: Figs. S5 and S6), indicating that the P-waves are reproduced well at short periods down to around 4 s. The residuals for the passband of 2–4 s are not sufficiently reduced in our analysis, because the passband is outside that of the FAMT analysis and the waveforms are not well constrained.

Discussion: sensitivity kernels

Through the FAMT analyses of the subduction-zone earthquakes, we have concluded that the seismic waveforms cannot be reproduced in the periods shorter than about 10 s, and the degree of fitting depends on the source locations, with better fittings for deep sources near land. These results indicate the necessity of improving the 3D structure model, especially for short-period waveforms from shallow sources far off the coast like EV2003. For this purpose, it would be helpful to study the regions where the waves propagate in the heterogeneous structure. In order to gain insights into the characteristics of such wave propagations, we employ an analysis based on the sensitivity kernel.

The sensitivity kernel has been used to study heterogeneities in the Earth's interior (Tarantola 1984; Tanimoto 1990; Tromp et al. 2005; Zhao et al. 2005; Yoshizawa and Kennett 2005). We use the method of Tanimoto and Okamoto (2014) to compute the waveform sensitivity kernels. The perturbation in a single component of the displacement in the frequency domain ($\delta u(\omega)$) can be expressed using the sensitivity kernels K_ρ, K_λ, and K_μ as follows:

$$\delta u(\omega) = \int_V \left[K_\rho(x,\omega) \left\{ \frac{\delta\rho(x)}{\rho(x)} \right\} + K_\lambda(x,\omega) \left\{ \frac{\delta\lambda(x)}{\lambda_0(x)} \right\} + K_\mu(x,\omega) \left\{ \frac{\delta\mu(x)}{\mu_0(x)} \right\} \right] dx, \quad (2)$$

(See figure on next page.)

Fig. 4 **a** Comparisons of the observed and synthetic velocity waveforms with several different passbands for EV2003. Here, we show the three components from two of the F-net broadband stations (TYS and HRO); for all thirty-three components, see Additional file 1: Fig. S3. The FAMT parameters are used to generate the synthetic waveforms. The passbands for each pair from top to bottom are 2–4, 4–7, 7–10, 10–15 and 4–40 s, respectively. The symbols "P" and "S" at the top traces denote the onsets of the *P*- and *S*-wave packets, respectively. **b** Same as **a** but for EV2007. For all forty-two components, see Additional file 1: Fig. S4. **c** The normalized residuals (F in Eq. 1) for EV2003. The residuals are computed using all the full waveforms of the 33 components with all the weights set to 1. Narrow-band cases are denoted by red squares, and broadband cases are denoted by blue squares. **d** Same as **c** but for EV2007. The residuals are computed using all the full waveforms of the 42 components

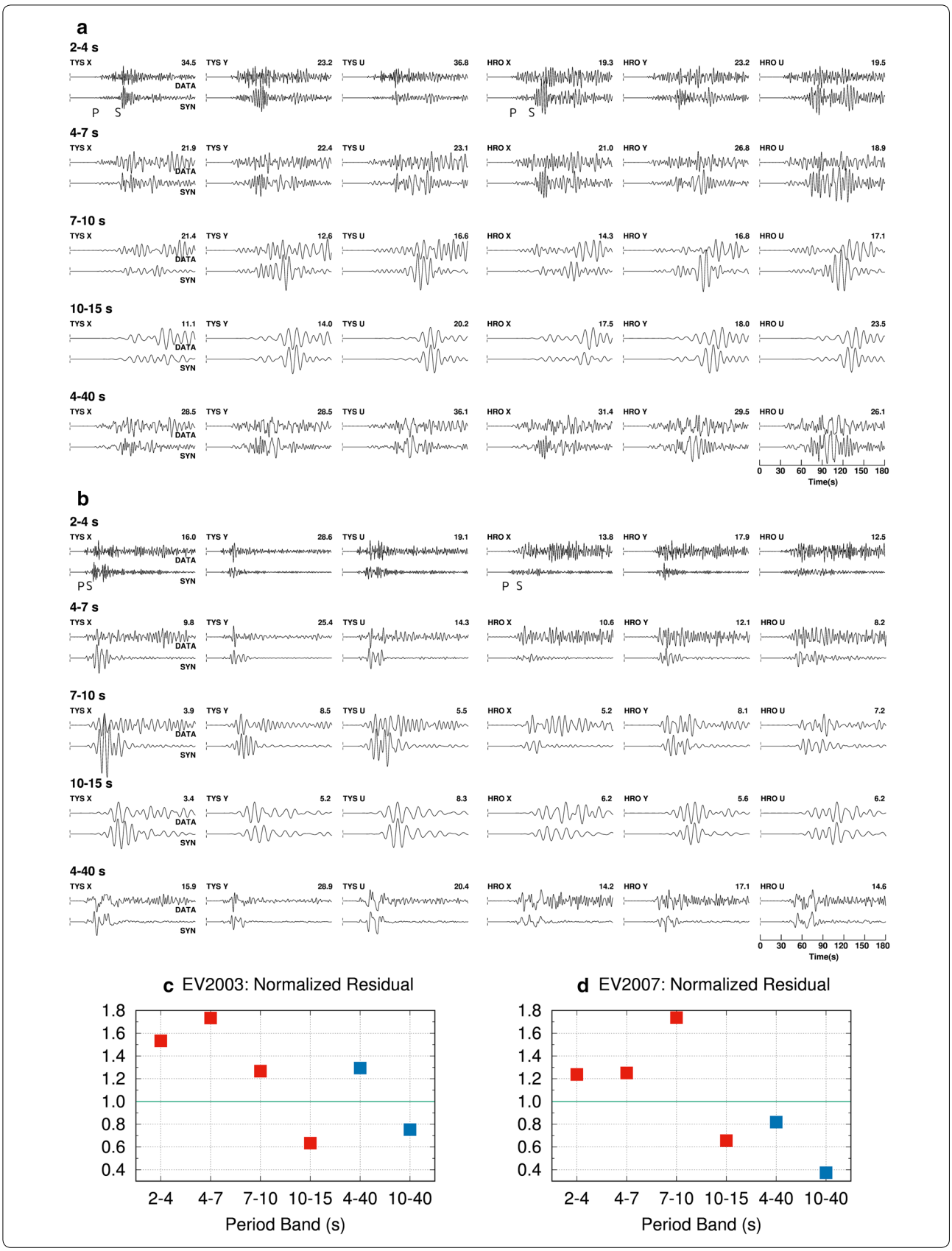
a
2-4 s
TYS X 34.5
TYS Y 23.2
TYS U 36.8
HRO X 19.3
HRO Y 23.2
HRO U 19.5
DATA
SYN
P S
4-7 s
TYS X 21.9
TYS Y 22.4
TYS U 23.1
HRO X 21.0
HRO Y 26.8
HRO U 18.9
7-10 s
TYS X 21.4
TYS Y 12.6
TYS U 16.6
HRO X 14.3
HRO Y 16.8
HRO U 17.1
10-15 s
TYS X 11.1
TYS Y 14.0
TYS U 20.2
HRO X 17.5
HRO Y 18.0
HRO U 23.5
4-40 s
TYS X 28.5
TYS Y 28.5
TYS U 36.1
HRO X 31.4
HRO Y 29.5
HRO U 26.1
0 30 60 90 120 150 180
Time(s)
b
2-4 s
TYS X 16.0
TYS Y 28.6
TYS U 19.1
HRO X 13.8
HRO Y 17.9
HRO U 12.5
P S
4-7 s
TYS X 9.8
TYS Y 25.4
TYS U 14.3
HRO X 10.6
HRO Y 12.1
HRO U 8.2
7-10 s
TYS X 3.9
TYS Y 8.5
TYS U 5.5
HRO X 5.2
HRO Y 8.1
HRO U 7.2
10-15 s
TYS X 3.4
TYS Y 5.2
TYS U 8.3
HRO X 6.2
HRO Y 5.6
HRO U 6.2
4-40 s
TYS X 15.9
TYS Y 28.9
TYS U 20.4
HRO X 14.2
HRO Y 17.1
HRO U 14.6
0 30 60 90 120 150 180
Time(s)
c EV2003: Normalized Residual
1.8
1.6
1.4
1.2
1.0
0.8
0.6
0.4
2-4 4-7 7-10 10-15 4-40 10-40
Period Band (s)
d EV2007: Normalized Residual
1.8
1.6
1.4
1.2
1.0
0.8
0.6
0.4
2-4 4-7 7-10 10-15 4-40 10-40
Period Band (s)

with

$$\left.\begin{aligned} K_\rho(x,\omega) &= \rho(x)\omega^2 \sum_i u_i^A(x,\omega)u_i(x,\omega), \\ K_\lambda(x,\omega) &= -\lambda_0(x)\Delta^A(x,\omega)\Delta(x,\omega), \\ K_\mu(x,\omega) &= -2\mu_0(x)\sum_{ij} e_{ij}^A(x,\omega)e_{ij}(x,\omega), \end{aligned}\right\} \quad (3)$$

where ρ denotes the density, λ_0 and μ_0 the reference elastic constants (relaxed moduli), μ_0 the rigidity, e_{ij} the strain tensor, and $\Delta = \sum e_{ii}$ (the above definitions are slightly different from that of Tanimoto and Okamoto (2014)). These kernels are computed from two wavefields: the forward wavefield computed with the earthquake source and the adjoint wavefield, which is denoted with the superscript A and computed with a single (impulsive) force placed at the station location (the direction of the force is the same as that of δu).

Here, we discuss the sensitivity kernels for the vertical component at station TYS for EV2003. We apply the FAMT parameters for the forward modeling of the seismic wavefield with a triangular moment rate time function with a base width of 2 s and a vertical single force with a triangular time function with a base width of 2 s at the station location for the adjoint wavefield. In computing the wavefield, we use the same method (GPU-accelerated HOT-FDM) as in the FAMT analyses. To avoid the singularity at the source location, we use a cosine-tapered finite source centered at the FAMT best location and distributed along the plate interface with a radius of 5 km for the forward wavefield. Further, we apply spatial smoothing to the raw kernels with a running average using a cell of 11.7 × 11.7 km horizontally and 6.3 km vertically. We apply a Fourier transform to the full synthetic waveforms with a duration of 250 s from the onset of the source application to obtain the components in the frequency domain. The real parts of the smoothed, normalized kernels thus computed are shown in Fig. 5. The kernel for a period of 12.8 s (Fig. 5a) displays a horizontal distribution nearly symmetric with respect to the straight path between the source and the station. This feature suggests a moderate effect of the heterogeneous structure, which results in the synthetics having a good fit to the observations for the long-period band ($\gtrsim$ 10s) waveforms. Also, the sensitive area extends to a relatively deep part (about 21 km deep), while the sensitivity in the shallow part (about 2 km deep) is relatively weak. On the other hand, the short-period kernel (6.1 s) shows a bend and has a spatially asymmetric pattern, which indicates a strong effect due to the 3D heterogeneous structure. A strong, shallow sensitive area in the depth range from 2 to 11 km for the period of 6.1 s indicates that shallow structures, such as sedimentary layers, are important in modeling short-period waveforms. Such a spatial pattern of sensitivity cannot be predicted with 1D Earth models and indicates the strong effects of 3D heterogeneity on short-period ($\lesssim$10s) waveforms. In addition, the cross-branch coupling between different mode branches would have a significant effect on the propagation of short-period surface waves in the period range treated in this study (e.g., Kennett and Nolet 1990; Marquering and Snieder 1995). Thus, it would be necessary to consider 3D effects such as curved paths and cross-branch coupling when improving the structure models. The finite-difference-based adjoint kernels displayed in this study incorporate all these effects and would be suitable for the study of the Earth's shallow structure.

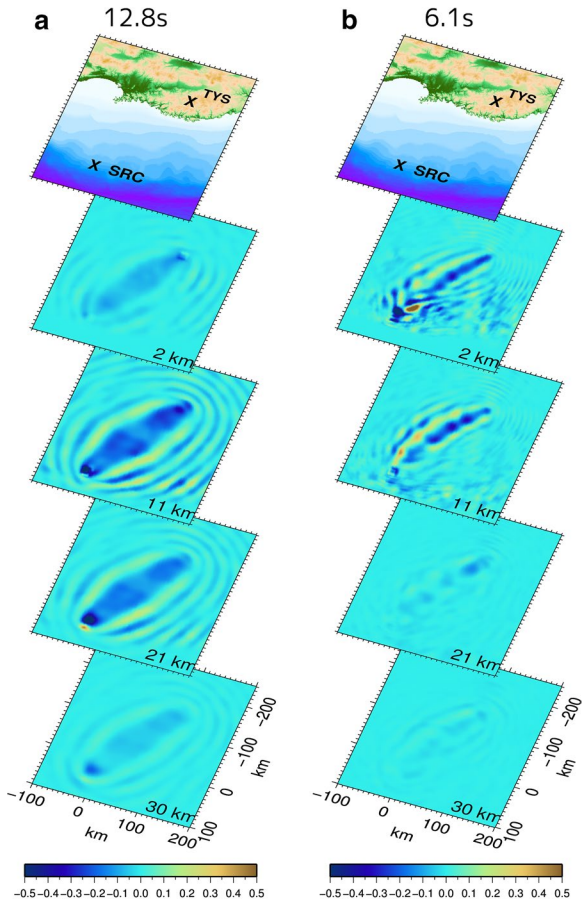

Fig. 5 Normalized, real part of rigidity kernels for period of **a** 12.8 s, and **b** 6.1 s, for the vertical component at station TYS (F-net). Crosses on the top map denote the locations of the FAMT solution (SRC) and the station (TYS), respectively. The horizontal slices of the three-dimensional kernels at depths of 2, 11, 21, and 30 km are displayed. The kernels are smoothed using a running average with a cell of 11.7 × 11.7 km horizontally and 6.3 km vertically, normalized with the maximum amplitude for each period, and clipped at a normalized amplitude of ± 0.5

Additional file

Additional file 1: Table S1. FDM parameters. **Table S2.** Estimated FAMT source parameters. **Table S3.** Estimated best double couples based on FAMT solutions. **Figure S1.** Residuals versus origin-time correction. **Figure S2.** Horizontal source locations estimated by the FAMT and other analyses. **Figure S3.** Comparisons of the observed and synthetic velocity waveforms for EV2003. **Figure S4.** Comparisons of the observed and synthetic velocity waveforms for EV2007. **Figure S5.** Comparisons of the first body wave part of the observed and synthetic velocity waveforms for EV2003. **Figure S6.** Comparisons of the first body wave part of the observed and synthetic velocity waveforms for EV2007.

Abbreviations

FDM: finite-difference method; 3D: three-dimensional; JMA: Japan Meteorological Agency; FAMT: first-motion augmented moment tensor; NIED: National Research Institute for Earth Science and Disaster Resilience; GCMT: global centroid moment tensor; GPU: graphic processing unit.

Authors' contributions

TN provided the model of the Philippine Sea plate. TO compiled the structure models for constructing the 3D structure model of the FDM simulations; coded the FDM program; performed the FDM simulation, inversion analysis, and sensitivity kernel analysis; and wrote the draft of the manuscript. HT and TN took part in discussions of the 3D structure model and the interpretation of the results of the inversion analyses. All authors contributed to the discussion and conclusions. All authors read and approved the final manuscript.

Author details

[1] Department of Earth and Planetary Sciences, Tokyo Institute of Technology, 2-12-1 Ookayama, Meguro, Tokyo 152-8551, Japan. [2] Department of Earth Sciences, Okayama University, 3-1-1 Tsushima-Naka, Kita-ku, Okayama 700-8530, Japan. [3] Earthquake and Tsunami Research Division, National Research Institute for Earth Science and Disaster Resilience, 3-1, Tennodai, Tsukuba, Ibaraki 305-0006, Japan.

Acknowledgements

The authors are grateful to JMA, NIED, and GCMT project for providing the earthquake parameters, to K Kisimoto and T Baba for providing the structure models, to NIED for providing the waveform records of K-NET, KiK-net, and F-net, and to M Takeo for providing the discrete wavenumber program. Comments by K Yoshizawa (editor) and two anonymous reviewers were very helpful in improving the manuscript.

Competing interests

The authors declare that they have no competing interests.

Availability of data and materials

The waveform data used in this study are available on the NIED Web site.

Consent for publication

Not applicable.

Ethics approval and consent to participate

Not applicable.

Funding

This study was supported by the Japan Society for the Promotion of Science (KAKENHI grant no.16K05535), HPCI System Research Project (Project ID: hp130118), and Joint Usage/Research Center for Interdisciplinary Large-scale Information Infrastructures in Japan (JHPCN) (Project ID: jh170022-NAJ).

Publisher's Note

Received: 31 December 2017 Accepted: 8 June 2018
Published online: 20 June 2018

References

Baba T, Ito A, Kaneda Y, Hayakawa T, Furumura T (2006) 3-D seismic wave velocity structures in the Nankai and Japan trench subduction zones derived from marine seismic surveys, Abstr Japan Geoscience Union Meet, S111-006, Makuhari, Japan

Fujiwara H, Kawai S, Aoi S, Morikawa N, Senna S, Kudo N, Ooi M, Hao K X-S, Hayakawa Y, Toyama N, Matsuyama H, Iwamoto K, Suzuki H, and Liu Y (2009) A study on subsurface structure model for deep sedimentary layers of Japan for strong-motion evaluation, Technical Note of the National Research Institute for Earth Science and Disaster Prevention, no. 337

Kennett BLN, Nolet G (1990) The interaction of the S-wavefield with upper mantle heterogeneity. Geophys J Int 101:751–762. https://doi.org/10.1111/j.1365-246x.1990.tb05581.x

Kisimoto K (2000) Combined bathymetric and topographic mesh data: Japan250 m.grd. Geological Survey of Japan, open-file report, no. 353

Marquering H, Snieder R (1995) Surface-wave mode coupling for efficient forward modelling and inversion of body-wave phases. Geophys J Int 120:186–208. https://doi.org/10.1111/j.1365-246x.1995.tb05920.x

Nakamura T, Okamoto T, Sugioka H, Ishihara Y, Ito A, Obana K, Kodaira S, Suetsugu D, Kinoshita M, Fukao Y, Kaneda Y (2010) 3D FDM simulation for very-low-frequency earthquakes off Kii Peninsula, Abstr Seism Soc Japan, P1-06, Hiroshima, Japan

Nakamura T, Takenaka H, Okamoto T, Kaneda Y (2012) FDM simulation of seismic-wave propagation for an aftershock of the 2009 Suruga bay earthquake: effects of ocean-bottom topography and seawater layer. Bull Seism Soc Am 102:2420–2435. https://doi.org/10.1785/0120110356

Nakamura T, Takenaka H, Okamoto T, Ohori M, and Tsuboi S (2015) Long-period ocean-bottom motions in the source areas of large subduction earthquakes. Sci Rep 5, Article number: 16648. https://doi.org/10.1038/srep16648

Okamoto T (2002) Full waveform moment tensor inversion by reciprocal finite difference Green's function. Earth Planets Space 54:715–720. https://doi.org/10.1186/bf03351723

Okamoto T, Takenaka H (2009) Waveform inversion for slip distribution of the 2006 Java tsunami earthquake by using 2.5D finite-difference Green's function. Earth Planets Space 61:e17–e20. https://doi.org/10.1186/bf03352919

Okamoto T, Takenaka H, Nakamura T, Aoki T (2010) Accelerating large-scale simulation of seismic wave propagation by multi-GPUs and three-dimensional domain decomposition. Earth Planets Space 62:939–942. https://doi.org/10.5047/eps.2010.11.009

Okamoto T, Takenaka H, Nakamura T, Aoki T (2013) Accelerating large-scale simulation of seismic wave propagation by multi-GPUs and three-dimensional domain decomposition. In: Yuen DA et al (eds) GPU solutions to multi-scale problems in science and engineering, chapter 24. Springer, Berlin. https://doi.org/10.1007/978-3-642-16405-7_24

Okamoto T, Takenaka H, Nakamura T, Hara T (2017) FDM simulation of earthquakes off western Kyushu, Japan, using a land–ocean unified 3D structure model. Earth Planets Space 69:88. https://doi.org/10.1186/s40623-017-0672-9

Takemura S, Shiomi K, Kimura T, Saito T (2016) Systematic difference between first-motion and waveform-inversion solutions for shallow offshore earthquakes due to a low-angle dipping slab. Earth Planets Space 68:149. https://doi.org/10.1186/s40623-016-0527-9

Takeo M (1985) Near-field synthetic seismograms taking into account the effects of anelasticity—the effects of anelastic attenuation on seismograms caused by a sedimentary layer. Pap Meteorol Geophys 36:245–257

Tanimoto T (1990) Modeling curved surface wave paths: membrane surface wave synthetics. Geophys J Int 102:89–100. https://doi.org/10.1111/j.1365-246x.1990.tb00532.x

Tanimoto T, Okamoto T (2014) The Millikan shaking experiments and high-frequency seismic wave propagation in Southern California. Geophys J Int 198:1081–1095. https://doi.org/10.1093/gji/ggu189

Tarantola A (1984) Inversion of seismic reflection data in the acoustic approximation. Geophysics 49:1259–1266. https://doi.org/10.1190/1.1441754

Tromp J, Tape C, Liu Q (2005) Seismic tomography, adjoint methods, time reversal and banana-doughnut kernels. Geophys J Int 160:195–216. https://doi.org/10.1111/j.1365-246x.2004.02453.x

Wu C, Koketsu K, Miyake H (2008) Source process of the 1978 and 2005 Miyagi-oki, Japan, earthquakes: repeated rupture of asperities over successive large earthquakes. J Geophys Res 113:B08316. https://doi.org/10.1029/2007jb005189

Yoshizawa K, Kennett BLN (2005) Sensitivity kernels for finite-frequency surface waves. Geophys J Int 162:910–926. https://doi.org/10.1111/j.1365-246x.2005.02707.x

Zhao L, Jordan TH, Olsen KB, Chen P (2005) Frechet kernels for imaging regional earth structure based on three-dimensional reference models. Bull Seism Soc Am 95:2066–2080. https://doi.org/10.1785/0120050081